

Structural and Dynamical Behaviors of Fast Ionic Conducting Potassium *nido*-(Carba)borates

Mads B. Amdisen,* Hui Wu,* Mikael S. Andersson, Mirjana Dimitrievska, Wei Zhou, Torben R. Jensen, Craig M. Brown, Juscelino B. Leão, and Terrence J. Udovic



Cite This: *Chem. Mater.* 2025, 37, 6450–6461



Read Online

ACCESS |



Metrics & More

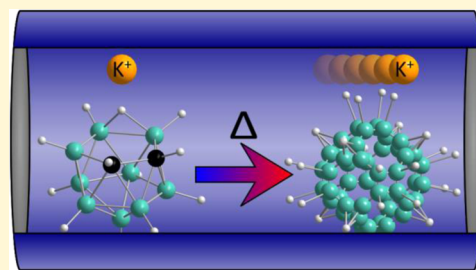


Article Recommendations



Supporting Information

ABSTRACT: Solid-state batteries are one of the most recent iterations of electrochemical energy storage, and the technology can potentially provide safer and more-energy-dense batteries. The metal *closo*- and *nido*-(carba)borates show promise as versatile solid electrolytes and have been shown to have some of the highest ionic conductivities as well as wide electrochemical stability windows. In the present study, we investigate the four potassium *nido*-(carba)borates $\text{KB}_{11}\text{H}_{14}$, $\text{K-7-CB}_{10}\text{H}_{13}$, $\text{K-7,8-C}_2\text{B}_9\text{H}_{12}$, and $\text{K-7,9-C}_2\text{B}_9\text{H}_{12}$, and a total of eight new crystal structures were solved. All four compounds transition from a low-temperature, ordered phase to a high-temperature, disordered phase with the space group $Fm\bar{3}m$. In the high-temperature polymorphs, the anions are disordered and undergo rapid reorientational dynamics, which is confirmed by quasielastic neutron scattering experiments. Reorientational activation energies of 0.151(2), 0.146(32), and 0.143(3) eV were determined for $\text{K-7-CB}_{10}\text{H}_{13}$, $\text{K-7,8-C}_2\text{B}_9\text{H}_{12}$, and $\text{K-7,9-C}_2\text{B}_9\text{H}_{12}$, respectively. Additionally, such rotationally fluid anions are concomitant with fast potassium-ion conductivity. The highest ionic conductivity is observed for $\text{K-7,8-C}_2\text{B}_9\text{H}_{12}$ with $1.7 \cdot 10^{-2} \text{ S cm}^{-1}$ at 500 K and an activation energy of 0.28 eV in the disordered state. The differences in phase transition temperatures, reorientational dynamics, and ionic conductivities among the potassium *nido*-(carba)borates illustrate a strong correlation between the K^+ cationic mobility and the local cation–anion interactions, anion dynamics, and the specific positions of the carbon atoms in the *nido*-(carba)borate anion cages.



INTRODUCTION

The rapidly growing demand for energy storage solutions for both mobile and stationary applications has prompted the development of technologies beyond conventional lithium-ion batteries. This is particularly apparent in the battery industry with a growing sodium-ion battery sector as well as a growing interest for solid-state batteries (SSB) due to the prospects of safer and more-energy-dense batteries.¹ While the ionic conductivity of solid-state electrolytes (SSE) is one of the major bottlenecks of SSBs,² recent developments in SSE research have shown that complex metal hydrides can have unparalleled ionic conductivities, even close to ambient conditions. Metal hydridoborates as SSEs have received significant attention since the discovery of the high ionic conductivity of the high-temperature polymorph of LiBH_4 , $\sigma(\text{Li}^+) \sim 10^{-3} \text{ S cm}^{-1}$.³ Since then, metal-hydridoborate-based SSEs have proliferated, and the employment of strategies such as the use of neutral ligands and hydridoborate cages with various shapes and sizes has increased in the search of an SSE that fulfills all SSB criteria.⁴

Extensive studies have revealed some of the highest ionic conductivities in the solid state for the alkali metal *closo*- and *nido*-(carba)borates, as well as wide electrochemical stability windows, making these materials some of the most promising metal hydridoborate-based SSEs.^{5,6} The *closo*- and *nido*-

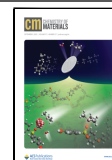
(carba)borate anions are large polyhedral boron–hydrogen cages such as $\text{B}_{12}\text{H}_{12}^{2-}$, $\text{CB}_{11}\text{H}_{12}^-$, $\text{B}_{11}\text{H}_{14}^-$, $\text{CB}_{10}\text{H}_{13}^-$, and $\text{C}_2\text{B}_9\text{H}_{12}^-$. A selection of the *nido*-(carba)borate anion cages are visualized in Figure 1. The differences in size, shape, and charge of the anions allow for great versatility in designing SSEs with tailored properties. Examples of this are the mixed anion superionic conductors $\text{Na}_2(\text{CB}_9\text{H}_{10})(\text{CB}_{11}\text{H}_{12})$ with an ionic conductivity of $\sigma(\text{Na}^+) \sim 7 \cdot 10^{-2} \text{ S cm}^{-1}$ at 300 K and $0.7\text{Li}(\text{CB}_9\text{H}_{10})\text{-}0.3\text{Li}(\text{CB}_{11}\text{H}_{12})$ with an ionic conductivity of $6.7 \cdot 10^{-3} \text{ S cm}^{-1}$ at 298 K.^{7,8} The electrochemical stability of these anions, $\text{CB}_9\text{H}_{10}^-$ and $\text{CB}_{11}\text{H}_{12}^-$, have been determined to be 3.55 V and $\sim 4.0 \text{ V}$ vs Li/Li^+ ,⁹ respectively, and 4.2 V vs Na/Na^+ ,¹⁰ respectively. While the electrochemical stability also depends on the cation, the generally high electrochemical stability of the larger borate cages, including the *nido*-borates [e.g., the electrochemical stability of $\text{B}_{11}\text{H}_{14}^-$ has been determined to be $\sim 2.6 \text{ V}$ vs Na/Na^+ (ref 5)], can potentially allow the use of moderately high-voltage cathodes.^{6,11}

Received: January 21, 2025

Revised: June 11, 2025

Accepted: June 12, 2025

Published: August 21, 2025



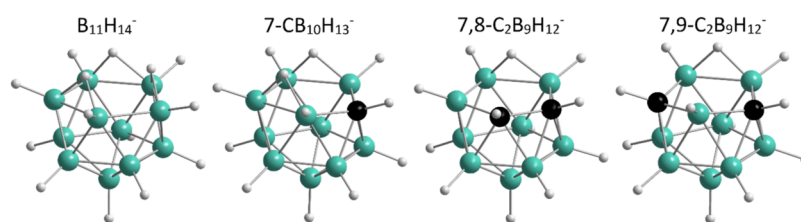


Figure 1. From left to right, the four different investigated *nido*-(carba)borate anions: Tetradecahydro-*nido*-undecaborate(1-) ($B_{11}H_{14}^-$), tridecahydro-*nido*-7-carbaundecaborate(1-) ($7-CB_{10}H_{13}^-$), dodecahydro-*nido*-7,8-dicarbaundecaborate(1-) ($7,8-C_2B_9H_{12}^-$), and dodecahydro-*nido*-7,9-dicarbaundecaborate(1-) ($7,9-C_2B_9H_{12}^-$). Color scheme: B (cyan), C (black), H (gray).

Furthermore, a $Na_4B_{10}H_{10}B_{12}H_{12}$ solid electrolyte has been reported to enable improved solid–solid interface contact and higher current density cycling.¹²

The high performance of the *closo*-(carba)borates has prompted investigations on their intrinsic properties to elucidate the mechanisms and effects behind the high ionic conductivities. In particular, investigations on carbon substitution of the $B_{12}H_{12}^{2-}$ cage have provided insights into the enhancing effects of breaking the symmetries of the borate cages.¹³ Carbon substitution introduces asymmetry and an anion dipole, which affects the local anion–cation interaction and reduces the charge, which also reduces the interaction strength between anion and cation.¹³ A similar effect is present in the metal *nido*-borates due to a missing atom in the icosahedral cage, which again can be further modified by the introduction of one or more carbon atoms.¹⁴

The high ionic conductivities are concomitant with fast anion reorientational dynamics. The fast dynamics in the *closo*- and *nido*-(carba)borates are typically introduced at elevated temperatures with a phase transition from a low-temperature ordered phase to a high-temperature disordered phase, similar to $LiBH_4$.^{14–18} Because of the dipole in the carborate and *nido*-borate anions, the anions have preferred orientations relative to the cations, which induces frustration in the crystal structures.^{13,14} Due to the otherwise high symmetry of the structures, the frustration leads to a complication of the phase transition to the low-temperature phase.¹³ Consequently, this effect can support a transition to a high-temperature, highly conductive phase at lower temperatures compared to the metal *closo*-borates, and also retain the high ionic conductivity to low temperatures.^{14–16} Other strategies to retain the high ionic conductivity at low temperatures, such as anion-mixing, ball-milling, and infiltration in nanoscaffold materials, have also been employed, but in most cases, these methods require a material with an already high ionic conductivity at elevated temperatures.^{19–22}

In the present study, we report the properties of the four potassium *nido*-(carba)borates $K-7,8-C_2B_9H_{12}$, $K-7,9-C_2B_9H_{12}$, $K-7-CB_{10}H_{13}$, and $KB_{11}H_{14}$, including the ionic conductivities as well as the concomitant anion reorientational dynamics determined from quasielastic and inelastic neutron scattering experiments. Eight new crystal structures were determined from *in situ* synchrotron radiation powder X-ray diffraction data, all in good agreement with temperature-dependent behaviors observed from electrochemical impedance spectroscopy, differential scanning calorimetry, and quasielastic neutron scattering.

EXPERIMENTAL SECTION

Four different potassium *nido*-(carba)borates ($K-7,8-C_2B_9H_{12}$, $K-7,9-C_2B_9H_{12}$, $K-7-CB_{10}H_{13}$, and $KB_{11}H_{14}$) were obtained from Katchem.²³

The different anions are shown schematically in Figure 1. Before all measurements, any residual water that may have been present was removed by a 16 h evacuation at 443 K for $K-7,8-C_2B_9H_{12}$, 433 K for both $K-7,9-C_2B_9H_{12}$ and $K-7-CB_{10}H_{13}$, and 383 K for $KB_{11}H_{14}$.

All four samples were screened for impurities with inductively coupled plasma optical emission spectrometry (ICP-OES). The samples were dissolved in a 1% nitric acid (HNO_3) solution made from 67–69% PlasmaPURE¹ HNO_3 and Milli-Q water. All samples were prepared as ~ 100 mg L^{-1} solutions to be able to detect small impurities. The high concentration entailed that the boron and potassium concentrations were outside the calibrated concentrations of the instrument, leading to some uncertainties. The measurements were carried out on a SPECTRO ARCOS inductively coupled plasma optical emission spectrometer instrument equipped with a Burgener Nebulizer and a Cyclonic Spray Chamber with an ASX-520 auto sampler.

Differential scanning calorimetry (DSC) measurements with thermogravimetric analysis (TGA) were made with a Netzsch (STA 449 F1 Jupiter). TGA-DSC measurements were conducted under He flow using finely ground samples in cold-weld-sealed Al sample pans. Heating/cooling rates were ± 5 $K\cdot min^{-1}$ for $KB_{11}H_{14}$ (2.0 mg), ± 20 $K\cdot min^{-1}$ for $K-7-CB_{10}H_{13}$ (9.9 mg), ± 20 $K\cdot min^{-1}$ and ± 10 $K\cdot min^{-1}$ for $K-7,9-C_2B_9H_{12}$ (3.7 mg), and ± 1 $K\cdot min^{-1}$ for $K-7,8-C_2B_9H_{12}$ (3.2 mg).

Synchrotron radiation powder X-ray diffraction (SRPX) patterns between 298 and 500 K were measured in sealed quartz capillaries at the Advanced Photon Source on Beamline 17-BM-B at Argonne National Laboratory [$\lambda = 0.45399(1)$ Å for $K-7,8-C_2B_9H_{12}$, $K-7,9-C_2B_9H_{12}$, and $K-7-CB_{10}H_{13}$; $\lambda = 0.45415(1)$ Å for $KB_{11}H_{14}$] using a two-dimensional amorphous Si-plate detector. The two-dimensional data were converted to one-dimensional data using GSAS-II.²⁴ Rietveld structural refinements²⁵ were performed using the GSAS package.²⁶ Additional *in situ* SRPX patterns of $K-7,8-C_2B_9H_{12}$, $K-7,9-C_2B_9H_{12}$, and $K-7-CB_{10}H_{13}$ between 298 and 500 K were measured in sealed borosilicate capillaries at MAX IV on the beamline DanMAX, $\lambda = 0.61992$ Å. Details on structural determination and Rietveld refinement are described in the Supporting Information (SI).

All neutron scattering measurements were performed at the National Institute of Standards and Technology Center for Neutron Research using thin samples to minimize neutron beam attenuation from the highly neutron-absorbing ^{10}B that comprises 20% of natural boron. Neutron vibrational spectroscopy (NVS) measurements at 4 K were done on the Filter-Analyzer Neutron Spectrometer (FANS)²⁷ using the Cu(220) monochromator with pre- and postcollimations of 20' of arc, yielding a full-width-at-half-maximum (fwhm) energy resolution of about 3% of the neutron energy transfer. Neutron-elastic-scattering fixed-window scans (FWSs) within temperature limits of 225 and 450 K were performed in heating and cooling regimes at ± 0.25 $K\cdot min^{-1}$ on the High-Flux Backscattering Spectrometer (HFBS),²⁸ which provides a resolution of 0.8 μeV fwhm using 6.27 Å wavelength incident neutrons. Quasielastic neutron scattering (QENS) measurements up to 550 K were done on the Disc Chopper Spectrometer (DCS),²⁹ utilizing incident neutron wavelengths of 4.8, 8, 8.5, and 9 Å with respective energies of 3.55, 1.28, 1.13, and 1.01 meV; respective resolutions of 56, 30, 26, and 22 μeV fwhm; and respective maximum attainable neutron

momentum transfer (Q) values of around 2.46, 1.48, 1.39, and 1.31 \AA^{-1} . The instrumental resolution function was obtained from the purely elastic QENS measurements, typically obtained at 100 K or below. All neutron data analyses were done with the DAVE software package.³⁰

Electrochemical impedance spectroscopy (EIS) data were measured with a 10 mV AC from 10 MHz to 1 Hz using a Bio-Logic MTZ-35 impedance analyzer equipped with a high-temperature sample holder. Sample pellets with a diameter of 5 mm and thicknesses between 1 and 2 mm were prepared at a mechanical pressure of 1 GPa. EIS data were analyzed with the software MT-Lab. The potassium ion conductivities, $\sigma(\text{K}^+)$, were calculated from the relation $\sigma = l R^{-1} A^{-1}$, where l and A are the height and area of the pellet, respectively. R is the resistance of the pellet determined by fitting a Debye-type circuit to the EIS data in a Nyquist plot. The activation energies were extracted from $\ln(\sigma T)$ vs T^{-1} plots.

To assist and complement the structural refinements and NVS measurements, first-principles calculations were performed within the plane-wave implementation of the generalized gradient approximation to Density Functional Theory (DFT) using a Vanderbilt-type ultrasoft potential with Perdew–Burke–Ernzerhof exchange correlation.³¹ A cutoff energy of 544 eV and a $2 \times 2 \times 2$ k -point mesh (generated using the Monkhorst–Pack scheme) were used and found to be enough for the total energy to converge within 0.01 meV/atom. All Rietveld structural refinements were performed with rigid-body anions, using their DFT energy-optimized structures. For comparison with the NVS measurements, the phonon densities of states (PDOS) were calculated for the DFT-optimized 0 K ordered structures using the supercell method with finite displacements^{32,33} and were appropriately weighted to take into account the H, K, B, and C total neutron scattering cross sections.

For all figures, standard uncertainties are commensurate with the observed scatter in the data, if not explicitly designated by vertical error bars.

RESULTS AND DISCUSSION

Initial Material Characterization. All four compounds, potassium tetradecahydrido-*nido*-7,8-dicarbaundecaborate(1-) ($\text{KB}_{11}\text{H}_{14}$), potassium tridecahydrido-*nido*-7-carbaundecaborate(1-) ($\text{K-7-CB}_{10}\text{H}_{13}$), potassium dodecahydrido-*nido*-7,8-dicarbaundecaborate(1-) ($\text{K-7,8-C}_2\text{B}_9\text{H}_{12}$), and potassium dodecahydrido-*nido*-7,9-dicarbaundecaborate(1-) ($\text{K-7,9-C}_2\text{B}_9\text{H}_{12}$) were characterized by nuclear magnetic resonance (NMR) spectroscopy and inductively coupled plasma optical emission spectrometry (ICP-OES) to determine their purity. $^{11}\text{B}\{^1\text{H}\}$ NMR spectra of $\text{KB}_{11}\text{H}_{14}$, $\text{K-7-CB}_{10}\text{H}_{13}$, $\text{K-7,8-C}_2\text{B}_9\text{H}_{12}$, and $\text{K-7,9-C}_2\text{B}_9\text{H}_{12}$ showed the expected resonances for all the anion cages with no indications of the presence of other boron-containing species; see Figure S1.^{34–37} ICP-OES experiments were conducted to determine the presence of other possible mobile cations and specifically Na, but showed no signs of impurities, see Table S1.

Thermal Behavior. Differential scanning calorimetry (DSC) was conducted to determine the polymorphic transition behavior of each compound, see Figure 2. During heating, a polymorphic transition is observed for all compounds, reproducible at the same temperature for multiple cycles. Additionally, a second transition is observed for $\text{K-7,9-C}_2\text{B}_9\text{H}_{12}$ at a higher temperature. However, the signal is significantly lower compared to the first transition indicating not much enthalpic difference between these phases, see the inset in Figure 2. Notably, there is little difference in the transition temperature of the compounds during heating, regardless of heating cycle and rate. The DSC data consistently shows hysteresis, but the transitions to the low-temperature polymorphs during cooling depend on the cycling parameters.

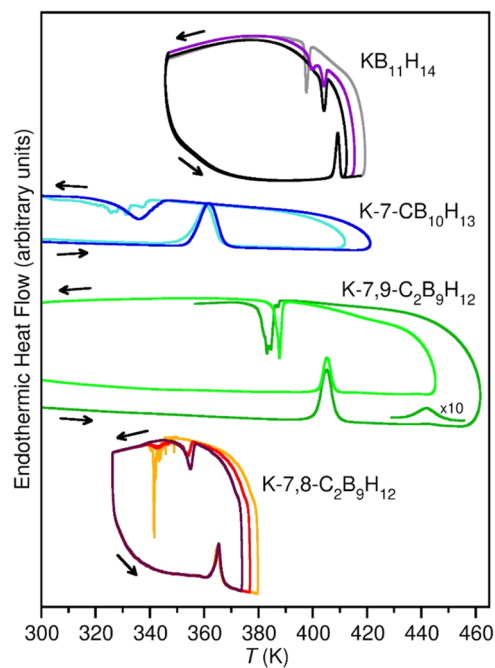


Figure 2. DSC data measured during heating and cooling for the potassium *nido*-(carba)borates. Data for each compound are scaled arbitrarily to facilitate the comparison between samples of different masses and heating/cooling rates. Heating and cooling segments are designated by the arrows. Sequential cycle numbers for each compound correspond to increasing maximum cycle temperatures. Color scheme: $\text{KB}_{11}\text{H}_{14}$ (black, gray, and purple), $\text{K-7-CB}_{10}\text{H}_{13}$ (blue and cyan), $\text{K-7,9-C}_2\text{B}_9\text{H}_{12}$ (dark-green (± 20 K $\cdot\text{min}^{-1}$) and light-green (± 10 K $\cdot\text{min}^{-1}$)), and $\text{K-7,8-C}_2\text{B}_9\text{H}_{12}$ (orange, red, and dark red).

Here, we also observe a transition of $\text{KB}_{11}\text{H}_{14}$ to its low-temperature polymorph at higher temperatures than observed by Souza et al.,³⁸ which may be due to a difference in purity. It is possible that the presence of K_2SO_4 in the sample made by Souza et al. has a stabilizing effect on the high-temperature polymorph.³⁸ Generally, if the compounds are cooled immediately after the high-temperature transition, a single relatively smooth transition to the low-temperature polymorph is observed. However, if the maximum temperature is increased slightly, or if the compound is held at the maximum temperature for an extended period, the cooling transition is shifted toward lower temperatures. Additionally, the cooling transitions become sporadic, which may be an indication of the differing thermal behaviors of various-sized crystallites in supercooled disordered states rapidly undergoing polymorphic transitions to ordered states. This possibly reflects changes in the structural quality and size of disordered-phase crystallites due to an annealing effect at elevated temperatures, which is sensitive to both time and temperature. The sporadic transitions are primarily observed for $\text{K-7-CB}_{10}\text{H}_{13}$ and $\text{K-7,8-C}_2\text{B}_9\text{H}_{12}$, see Figure 2.

Structural Investigations. Eight new crystal structures were determined from SRPX data. Unit cell parameters and Rietveld refinements are provided in Table 1 and Figures S2–S10 respectively.

Crystal Structure of Potassium Tetradecahydrido-*nido*-undecaborate(1-). The low-temperature structure of potassium tetradecahydrido-*nido*-undecaborate(1-), here denoted potassium *nido*-borate, α - $\text{KB}_{11}\text{H}_{14}$, has previously been determined with the triclinic space group $P-1$,³⁸ and our

Table 1. Crystallographic Data Extracted by Rietveld Refinement

compound	space group	axial lengths (Å)	axial angles (°)	V (Å ³)	T (K) ^a
α -KB ₁₁ H ₁₄	<i>P</i> -1	$a = 7.1933(4)$ $b = 7.0472(5)$ $c = 19.4074(9)$	$\alpha = 90.715(4)$ $\beta = 85.951(4)$ $\gamma = 90.009(4)$	981.28(13)	298
β -KB ₁₁ H ₁₄	<i>Fm</i> -3 <i>m</i>	$a = 10.1809(5)$	-	1055.24(16)	418
α -K-7-CB ₁₀ H ₁₃	<i>P</i> 2 ₁ / <i>a</i>	$a = 18.8457(6)$ $b = 6.9700(3)$ $c = 7.2334(3)$	$\beta = 91.269(3)$	949.91(8)	298
β -K-7-CB ₁₀ H ₁₃	<i>Fm</i> -3 <i>m</i>	$a = 10.0713(4)$	-	1021.54(12)	415
α -K-7,8-C ₂ B ₉ H ₁₂	<i>P</i> 2 ₁ / <i>n</i>	$a = 10.0499(4)$ $b = 12.6135(6)$ $c = 7.33361(31)$	$\beta = 91.0011(24)$	929.49(10)	298
β -K-7,8-C ₂ B ₉ H ₁₂	<i>Fm</i> -3 <i>m</i>	$a = 10.0115(10)$	-	1003.47(31)	420
α -K-7,9-C ₂ B ₉ H ₁₂	<i>P</i> 2 ₁ / <i>a</i>	$a = 10.7796(4)$ $b = 11.4692(4)$ $c = 7.43895(27)$	$\beta = 93.5186(16)$	917.97(8)	298
β -K-7,9-C ₂ B ₉ H ₁₂	<i>P</i> -31 <i>c</i>	$a = 6.9728(7)$ $c = 11.7364(10)$	-	494.18(12)	444
γ -K-7,9-C ₂ B ₉ H ₁₂	<i>Fm</i> -3 <i>m</i>	$a = 10.0363(4)$	-	1010.93(14)	500

^aData collection temperature.

results are in agreement with this structure. Each K⁺ cation is surrounded by six B₁₁H₁₄⁻ anions, forming an octahedral coordination geometry. The cation is slightly shifted from the center of the ideal octahedral position due to the dipole of the anion. With a higher positive charge at the nest-end of the anion,^{14,16} the anion has a preferred orientation with the nest-end pointing away from the cation. As all octahedral positions are occupied, the preferred orientation of the anion cannot be fulfilled, resulting in the cation being pushed toward one of the edges of the octahedron. The compound undergoes a first-order phase transition to its high-temperature polymorph, β -KB₁₁H₁₄, at ~ 405 K. The high-temperature polymorph has previously³⁸ been indexed in the space group *Fm*-3*m*, and the space group of the structure determined here is in agreement with this result; see Table 1. The cubic structure is a result of the almost isotropic disordering of the anion on the diffraction time scale and is similar to several other *fcc* metal *nido*- and *closo*-(carba)borates; see Figure 3b.

Crystal Structure of Potassium Tridecahydrido-*nido*-7-carbaundecaborate(1-). Potassium tridecahydrido-*nido*-7-carbaundecaborate(1-), α -K-7-CB₁₀H₁₃, crystallizes in a monoclinic unit cell with space group *P*2₁/*a*. Each K⁺ cation is surrounded by six 7-CB₁₀H₁₃⁻ anions, forming an octahedral coordination geometry. As for the B₁₁H₁₄⁻ anion, a higher localized positive charge is located at the nest-end of the 7-CB₁₀H₁₃⁻ anion. The carbon atom is part of the nest-end of the anion. Carbon substitution of boron atoms in the anion cages changes the charge distribution as observed for previously calculated Mulliken charges of isolated *nido*- and *closo*-carbaborate anions.^{14–16,39} Due to the higher electronegativity of carbon compared to boron, hydrogen atoms bonded to carbon have larger positive Mulliken charges relative to the rest of the hydrogen atoms in the cages.¹⁴ This also results in a preferred orientation of the anion with the nest-end pointing away from the cation. Consequently, the cation is pushed toward one of the faces of the octahedron. α -K-7-CB₁₀H₁₃ undergoes a first-order transition to a *fcc*-type high-temperature polymorph, β -K-7-CB₁₀H₁₃, at ~ 345 K, with space group *Fm*-3*m*; see Figures 2 and S11. The anions are described by almost isotropic disordering on the diffraction time scale, and the cations are positioned in the ideal octahedral positions.

Crystal Structure of Potassium Dodecahydrido-*nido*-7,8-dicarbaundecaborate(1-). Potassium dodecahydrido-*nido*-7,8-dicarbaundecaborate(1-), α -K-7,8-C₂B₉H₁₂, crystallizes in a monoclinic unit cell with space group *P*2₁/*n*. Similar to the two aforementioned structures, each K⁺ cation is surrounded by six 7,8-C₂B₉H₁₂⁻ anions, forming an octahedral coordination

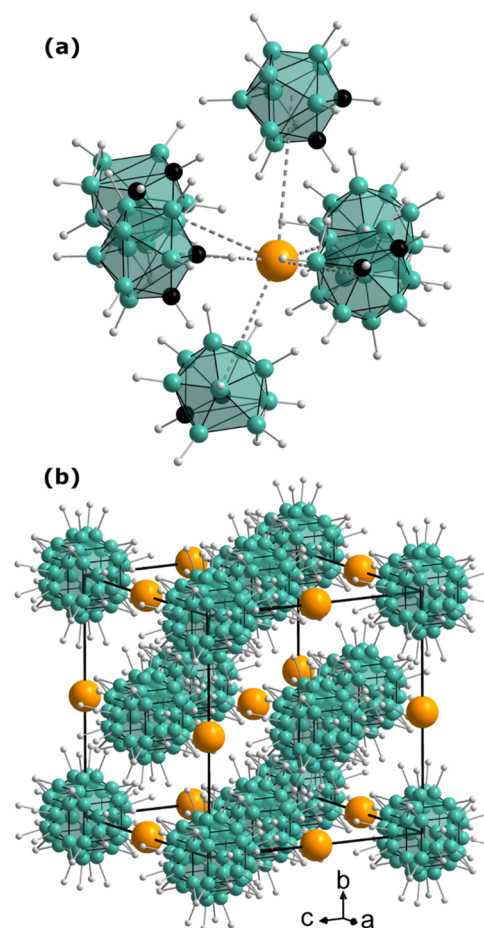


Figure 3. (a) Octahedral coordination environment of K⁺ in α -K-7,8-C₂B₉H₁₂ (*P*2₁/*n*). (b) Representation of the high-temperature structures with space group symmetry *Fm*-3*m*. The disordered anions are a single color because C and B are indistinguishable. Color scheme: K⁺ (orange), B (cyan), C (black), H (gray).

geometry. With an additional carbon atom, a slightly greater localized positive charge is situated on the nest-end of the 7,8-C₂B₉H₁₂⁻ anion as compared to 7-CB₁₀H₁₃⁻.¹⁴ Again, this results in a preferred orientation of the anion with the nest-end pointing away from the cation, and the cation is pushed toward one of the faces of the octahedron; see Figure 3a. α -K-7,8-C₂B₉H₁₂ undergoes a first order transition to a similar *fcc*-type high-temperature polymorph, β -K-7,8-C₂B₉H₁₂, in space group *Fm*-3*m*, at ~ 360 K; see Figure S11. The anions are described by almost isotropic disordering on the diffraction time scale,

and the cations are positioned in the ideal octahedral positions; see Figure 3b.

Crystal Structure of Potassium Dodecahydrido-nido-7,9-dicarbaundecaborate(1-). Potassium dodecahydrido-nido-7,9-dicarbaundecaborate(1-), α -K-7,9-C₂B₉H₁₂, crystallizes in a monoclinic unit cell with space group $P2_1/a$. Similar to the structures of the three aforementioned potassium nido-(carba)borates, each K⁺ cation is surrounded by six 7,9-C₂B₉H₁₂⁻ anions, forming an octahedral coordination geometry. A slightly greater localized positive charge is situated on the nest-end of the 7,9-C₂B₉H₁₂⁻ anion compared to the 7,8-C₂B₉H₁₂⁻, which suggests that the position and possibly the flexibility of the hydrogen atoms influences the local charge.¹⁴ This results in a preferred orientation of the anion with the nest-end pointing away from the cation, and the cation is pushed toward one of the faces of the octahedron. Two polymorphic transitions are observed for K-7,9-C₂B₉H₁₂. An intermediate structure, β -K-7,9-C₂B₉H₁₂, is observed during the polymorphic transition from the ordered low-temperature monoclinic structure α -K-7,9-C₂B₉H₁₂ to the fully disordered high-temperature cubic structure γ -K-7,9-C₂B₉H₁₂. The polymorphic transition from α -K-7,9-C₂B₉H₁₂ to β -K-7,9-C₂B₉H₁₂ is a first-order transition occurring at \sim 395 K, whereas the transition from β -K-7,9-C₂B₉H₁₂ to γ -K-7,9-C₂B₉H₁₂ is a second-order transition occurring from \sim 450 to \sim 500 K, consistent with DSC data; see Figure S11. The intermediate β -K-7,9-C₂B₉H₁₂ crystallizes in a trigonal unit cell with space group $P\bar{3}1c$, resembling the high-temperature structure of Na-7,8-C₂B₉H₁₂ ($P\bar{3}1c$) as well as LiCB₉H₁₀ ($P\bar{3}1c$).^{14,15} The high-temperature γ -K-7,9-C₂B₉H₁₂ forms a cubic structure with the space group $Fm\bar{3}m$ similar to the rest of the high-temperature potassium nido-(carba)borates. Disorder of the anions are observed in both β - and γ -K-7,9-C₂B₉H₁₂. The average structures on the diffraction time scale derived from the refinement revealed that a simple isotropic icosahedron can sufficiently describe the randomly orientated 7,9-C₂B₉H₁₂ anions in the β -phase while these disorderly orientated anions would be better described by an isotropic sphere in the γ -phase; see Figure 3, indicating a faster rotation of the anions at higher temperatures. In addition, the disordered anions in the β -phase arrange themselves into an hcp stacking (ABAB...) whereas they adopt an fcc stacking (ABCABC...) in the γ -phase. Such structural variations are consistent with the phase transitions observed in DSC and *in situ* XRD, i.e., a first-order phase transition from the α - to the β -phase, which is an order-to-disorder structural transition, and a weak enthalpic second-order transition from the β - to the γ -phase, which only involves a small stacking sequence rearrangement and the rotational rate changes of anions.

Besides the direct visualization of the structural changes in the *in situ* synchrotron X-ray diffraction patterns collected across the phase-transition-temperature ranges (Figure S11a), Rietveld refinements were also conducted on diffraction patterns before and after the transition temperature to confirm the lattice changes upon phase transition, and plots of formula unit volume (i.e., unit cell volume/ Z) vs T for K-B₁₁H₁₄ and K-7,9-C₂B₉H₁₂ are shown in Figure S11b. The formula unit volumes of these compounds were found to slightly increase with temperature in the temperature range of the ordered α -phase due to the lattice thermal expansion. As expected, when the order-to-disorder phase transition occurs, the formula unit volume exhibits an abrupt jump, consistent with the previous reports on the high-temperature disordered structures of the

(carba)borates, where the rearrangement of the large anions creates more spacious open channels for cations to migrate,^{15–17,38,39} and also concurring with the surge of potassium ionic conductivity at high temperatures (see Figure 8). The lattice changes upon phase transition of K-7-CB₁₀H₁₃ and K-7,8-C₂B₉H₁₂ exhibit a similar trend to that of KB₁₁H₁₄ as they all possess a similar first-order transition to the high-temperature fcc-type disordered structure. For K-7,9-C₂B₉H₁₂, the structural change from the ordered monoclinic α -phase to the disordered trigonal β -phase is a first-order phase transition. Therefore, a sudden upturn in formula unit volume is expected and indeed observed around the transition temperature. While the structural change from the disordered β -phase to the disordered γ -phase is a second-order transition that only involves changes in the anion stacking sequence and anion rotational rate. Therefore, as shown in the change of K-7,9-C₂B₉H₁₂ formula unit volume, it is a slow process for the β -phase to completely transform to the γ -phase, and these two phases coexist with varying phase fractions upon increasing temperature. Over the studied temperature range of the disordered state, the formula unit volumes of these two disordered phases follow a similar trend, i.e., both increase with temperature but with a slightly higher increasing rate for the trigonal β -phase thanks to more expansion along the c direction of its unit cell to accommodate the anion stacking rearrangement, and finally they become almost the same at 500 K when β -phase nearly completes the transformation to γ -phase i.e., 98 wt % as shown in Figure S10. In addition to the formula unit volume change with temperature, we also observed a similar changing trend in the thermal parameters of the K⁺ cation and nido-(carba)borate anion with increasing temperature. For example for K-7,9-C₂B₉H₁₂, the thermal parameter of potassium in the ordered α -phase shows a mild increase with temperature, e.g., $U_{\text{iso}}(\text{K}) \sim 0.052(3) \text{ \AA}^3$ at 298 K, $\sim 0.058(3) \text{ \AA}^3$ at 368 K, and $\sim 0.068(3) \text{ \AA}^3$ at 391 K, followed by a significant upturn when the ordered α -phase transforms to the disordered β -phase, e.g., $U_{\text{iso}}(\text{K}) \sim 0.35(3) \text{ \AA}^3$ at 444 K. Afterward, the changes in the thermal factors of K are very small and within the estimated standard deviation (e.s.d.) over the measured high temperatures. The thermal parameters of B(C) atoms in the C₂B₉H₁₂ anions in the ordered α -phase exhibit little change with temperature (i.e., magnitudes of the changes are within e.s.d.). Upon phase transition to the disordered β -phase, the magnitude of the thermal parameters of B noticeably increases, e.g., from $U_{\text{iso}}(\text{B}) \sim 0.027(5) \text{ \AA}^3$ in the range of 298–410 K to $U_{\text{iso}}(\text{B}) \sim 0.16(8) \text{ \AA}^3$ in the range of 420–500 K. Although the exact values of the thermal parameters of K⁺ cations and anions over the measured high-temperature ranges may not be able to be accurately determined as they were observed to not noticeably affect R -factors during the refinement because of the high temperature and structural disordering, the changes in the magnitude of thermal parameters across the phase transition should be trustworthy. Nevertheless, the observed surge in the thermal parameters of K and B at the order-to-disorder phase transition is in accord with the formula unit volume change as well as the thermal events observed in DSC curves.

The potassium nido-carbaborates in the present study all crystallize in similar monoclinic structures with space group $P2_1/a$ or $P2_1/n$ at room temperature. In comparison, the sodium nido-carbaborates are structurally slightly different with Na-7-CB₁₀H₁₃ and Na-7,9-C₂B₉H₁₂ crystallizing in orthorhombic unit cells, with the exception of Na-7,8-C₂B₉H₁₂, which also

crystallizes in a monoclinic unit cell.¹⁴ The difference in symmetry between the sodium and potassium *nido*-carbaborates suggests that the larger K⁺ cation induces lower symmetry in the crystal structures.¹⁴ A similar effect has been observed for the sodium and potassium *closo*-dodecacarbaborates.^{16,39} The valence and the shape of the anion as well as the charge distribution over the cage are also highly influential on the symmetry of the structure and the cation coordination environment. With the icosahedral B₁₂H₁₂²⁻ anion cages, potassium *closo*-dodecaborate crystallizes in a cubic unit cell with K⁺ cations occupying all the tetrahedral holes, whereas the monovalent *closo*-dodecacarbaborate anion, CB₁₁H₁₂⁻, entails an octahedral K⁺ coordination environment instead, due to a dilution of the cations.^{39,40} The *nido*-(carba)borate anions are generally monovalent and consequently also form structures with one cation per formula unit. Carbon substitution of boron atoms in the anion cages changes the charge distribution as observed for previously calculated Mulliken charges of isolated *nido*- and *closo*-carbaborate anions.^{14–16,39} Due to the higher electronegativity of carbon compared to boron, hydrogen atoms bonded to carbon have larger positive Mulliken charges relative to the rest of the hydrogen atoms in the cages.¹⁴ Directionality of the charge on the anions causes a preferred orientation relative to the cations, with the more positive hydrogen atoms maximizing their distance to the cations.^{16,41}

Bonding Interactions. The vibrational dynamics of the four *nido*-compounds were characterized by neutron vibrational spectroscopy (NVS) at 4 K. The neutron vibrational spectra are shown in Figure 4 in comparison with the simulated one+two-phonon densities of states of the corresponding DFT-optimized, low-temperature, ordered structures and the isolated anions. The spectrum in the measured energy region is dominated by the normal modes involving the different anion deformations. More intense vibrational features reflect normal modes with more significant H atom displacements due to the much larger neutron scattering cross-section as well as generally larger vibrational amplitudes for H atoms compared to the other elements present. As the vibrational signature of polyhedral (carba)-borate-based salt compounds is typically sensitive to the particular structural arrangement,⁴² the reasonably good agreement between the experimental and simulated spectra for all four compounds corroborates the low-*T* ordered structures determined by SRPX. The poorer agreement with the isolated anion spectra confirms the importance of lattice effects on the measured PDOS. Further information about the characters and energies of the different phonon modes contributing to the simulated PDOS for the four *nido*-compounds can be found in the animation files in the Supporting Information.⁴³

Anion Reorientational Dynamics. Fixed Window Scans. A change in the reorientational dynamics of the anions is also evident from a neutron elastic scattering fixed window scan (FWS). By integrating a fixed-energy slice centered around the elastic peak for each temperature, it is possible to monitor the temperature-dependent evolution of the *nido*-(carba)borate anions due to the large incoherent scattering cross-section of the hydrogen bound to the cages. When the jump frequencies increase above $\sim 10^8$ jumps s⁻¹, the elastic peak begins to broaden quasielastically, which means the intensity in the integrated region decreases. When the quasielastic part becomes so broad that it no longer contributes to the integrated region (above $\sim 10^{10}$ jumps s⁻¹), the temperature-

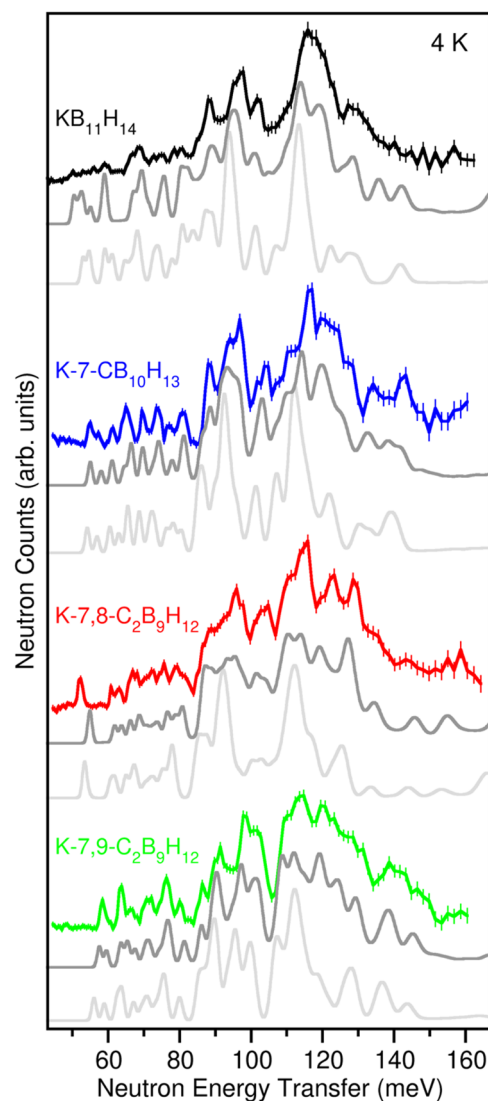


Figure 4. Neutron vibrational spectra of KB₁₁H₁₄ (blue), K-7-CB₁₀H₁₃ (green), K-7,8-C₂B₉H₁₂ (red), and K-7,9-C₂B₉H₁₂ (violet) at 4 K compared to the simulated one+two-phonon densities of states of the corresponding DFT-optimized, low-*T*, ordered structures (dark gray) and the isolated anions (light gray). Vertical error bars represent $\pm 1\sigma$. (N.B., 1 meV \approx 8.0655 cm⁻¹).

dependent evolution of the dynamics can no longer be probed with the FWS.¹⁴ A more detailed description of the FWS technique can be found in refs 44 and 45.

All four potassium *nido*-(carba)borates exhibit hysteresis, similar in magnitude to the results from DSC, of the anion dynamics based on the FWSs; see Figure 5. The transitions during heating happen within a narrow temperature range, 5–20 K, whereas the transitions during cooling are slightly slower. The FWSs of KB₁₁H₁₄ and K-7-CB₁₀H₁₃ initially decrease more rapidly than the FWSs of K-7,8-C₂B₉H₁₂ and K-7,9-C₂B₉H₁₂, suggesting that minor dynamics are introduced at lower temperatures in the two former compounds, consistent with their larger unit cell volumes at 298 K. The smaller Mulliken charges on the nest-end hemisphere of the non- and monocarbon-substituted anions compared to the disubstituted anions may also contribute to less directionality of the anions.¹⁴ The rapid decrease in intensity, and thereby increase in anion dynamics, of each compound during heating happens

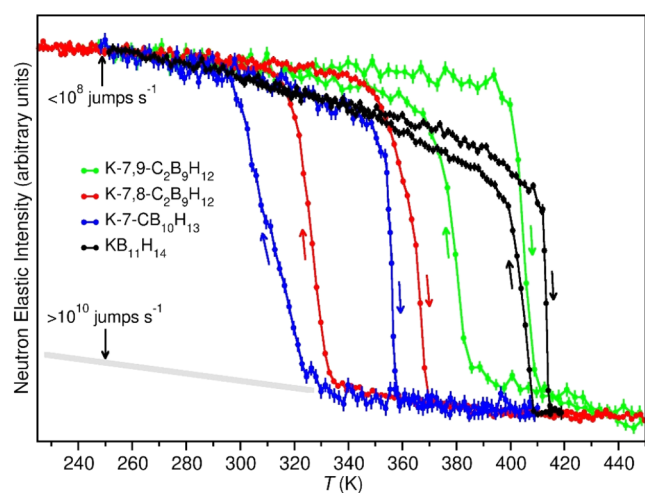


Figure 5. Neutron fixed window scans of the four potassium *nido*-(carba)borates. The heating and cooling directions are displayed with arrows.

in the order K-7-CB₁₀H₁₃ (~ 345–360 K), K-7,8-C₂B₉H₁₂ (~ 345–370 K), K-7,9-C₂B₉H₁₂ (~ 395–410 K), and KB₁₁H₁₄ (~ 405–415 K); see Figure 5, consistent with the first-order phase transitions observed from DSC and *in situ* SRPXD. K-7-CB₁₀H₁₃ and K-7,8-C₂B₉H₁₂ show high similarity in their transition temperatures with the K-7,8-C₂B₉H₁₂ transition temperature range being approximately 10 K wider. A similar behavior has been observed for the equivalent sodium salts.¹⁴ K-7,9-C₂B₉H₁₂ undergoes a more rapid transition than K-7,8-C₂B₉H₁₂, but at a 50 K higher temperature, whereas the two equivalent sodium salts reach the detection limit almost simultaneously. From *in situ* SRPXD data, β -K-7,9-C₂B₉H₁₂ is the dominating phase to ~ 450 K (see Figure S11), while γ -K-7,9-C₂B₉H₁₂ is the dominating phase at 500 K. Two wt % of β -K-7,9-C₂B₉H₁₂ persists at 500 K, which emphasizes the slow transition to fully disordered anion cages compared to the rapid transition of K-7,8-C₂B₉H₁₂. Additionally, the K-7,9-C₂B₉H₁₂ dynamics do not reach the detection limit at 410 K after the first phase transition from α -K-7,9-C₂B₉H₁₂ to β -K-7,9-C₂B₉H₁₂. However, after the initial intensity drop, a slow decrease in intensity is observed from 410 K, consistent with the second phase transition from β -K-7,9-C₂B₉H₁₂ to γ -K-7,9-C₂B₉H₁₂.

Anion dynamics for potassium *nido*-borate, KB₁₁H₁₄, undergo rapid changes during both heating and cooling. The anion dynamics reach the detection limit at ~ 415 K during heating and rapidly slow down again from ~ 410 K during cooling. In comparison, NaB₁₁H₁₄ transitions to both the disordered and the ordered state at temperatures lower than the two sodium *nido*-carbaborates, Na-7,8-C₂B₉H₁₂ and Na-7,9-C₂B₉H₁₂.¹⁴ This suggests that the larger potassium cation favors carbon substitution in the anion cages in terms of improved rotational dynamics at lower temperatures compared to the sodium salts.

Quasielastic Neutron Scattering. Quasielastic neutron scattering experiments were done for all four compounds in their high-temperature disordered polymorph phases, starting at the highest temperature and sequentially cooling down. Typically, one can extract jump correlation frequencies τ^{-1} associated with the Lorentzian components of the quasielastic spectra via the relation $\tau^{-1} = \Gamma/(2\hbar)$ (where Γ is the Lorentzian full-width-half-maximum (fwhm) line width and \hbar

is the reduced Planck's constant). The temperature dependence of the fundamental jump correlation frequency τ_1^{-1} is shown in Figure 6. The τ_1^{-1} values were typically extracted

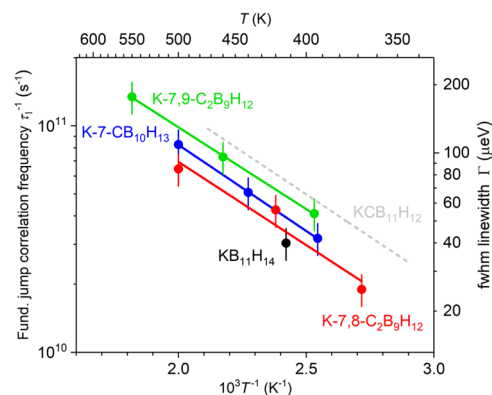


Figure 6. Fundamental jump correlation frequencies τ_1^{-1} of KB₁₁H₁₄ (black), K-7-CB₁₀H₁₃ (blue), K-7,8-C₂B₉H₁₂ (red), and K-7,9-C₂B₉H₁₂ (green) as a function of temperature compared to the behavior previously reported for KCB₁₁H₁₂.³²

from the QENS spectra using incident neutron wavelengths of 8, 8.5, or 9 Å at $Q = 0.8 \text{ \AA}^{-1}$, where there is minimal contamination from higher-order Lorentzian components.¹⁰ Exemplary QENS spectra and fits are displayed in Figure S12 of the SI. All disordered polymorphs exhibit comparable τ_1^{-1} values in the range of 10^{10} – 10^{11} jumps·s⁻¹ between 365 and 550 K. Reorientational activation energies E_a were determined from the slope ($-E_a/k_B$) of the linear fit of $\ln(\tau_1^{-1})$ vs T^{-1} , where k_B is the Boltzmann constant. Values of 0.151(2), 0.146(32), and 0.143(3) eV were determined for K-7-CB₁₀H₁₃, K-7,8-C₂B₉H₁₂, and K-7,9-C₂B₉H₁₂, respectively. We note that the value for K-7,9-C₂B₉H₁₂, although similar to those for the other compounds, may have been affected by the presence of the intermediate disordered β -K-7,9-C₂B₉H₁₂ at the lower temperatures measured. Nonetheless, no further effort was made to distinguish separate activation energies for β -K-7,9-C₂B₉H₁₂ and γ -K-7,9-C₂B₉H₁₂. The reported E_a values for the *nido*-carbaborates are in line with 0.149(2) eV reported for the *closo*-carbaborate KCB₁₁H₁₂, although as seen from Figure 6, the τ_1^{-1} values for the *nido*-borates are somewhat less than for *closo*-KCB₁₁H₁₂ at the same temperatures. We note that no E_a value for KB₁₁H₁₄ could be extracted since its jump correlation frequency was only measured at one temperature near its transition point ($\sim 3 \times 10^{10}$ jumps·s⁻¹ at 413 K), higher-temperature measurements being discouraged by the lengthy measurement time required coupled with the relatively more thermally unstable nature of this particular compound. A previous NMR study of KB₁₁H₁₄ dynamics⁴⁶ indicated a similar jump frequency and an E_a value of 0.19(3) eV for the disordered β -phase in the 400 K–418 K region. In contrast, the jump frequency for the ordered α -phase at 393 K just below the transition was found to be two-orders of magnitude lower ($\sim 10^8$ s⁻¹) with a substantially higher E_a value of 0.53(2) eV.⁴⁶

Further details concerning the anion reorientational mechanism in the disordered phases can be gleaned from the Q -dependent behavior of the elastic incoherent structure factor (EISF), which is defined as the ratio of the elastic scattering intensity to the total scattering intensity (i.e., elastic + quasielastic intensity). The experimental EISF results for β -

K-7,8-C₂B₉H₁₂ at 500 K, γ -K-7,9-C₂B₉H₁₂ at 550 K, and β -K-7-CB₁₀H₁₃ at 500 K versus Q are exemplified in Figure 7 and

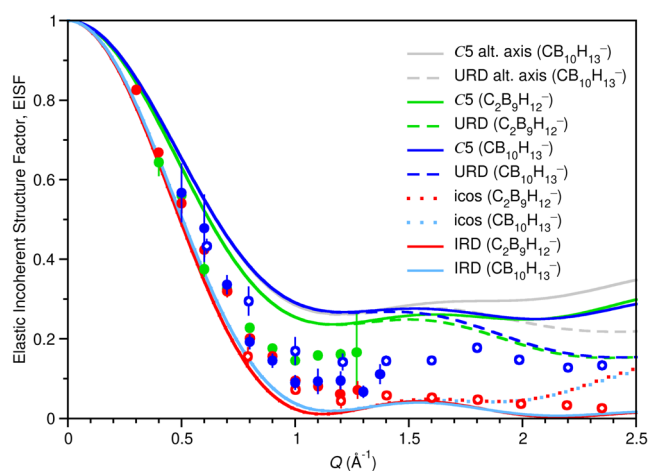


Figure 7. Elastic incoherent structure factors as functions of Q for K-7-CB₁₀H₁₃ (500 K, blue symbols, filled: 8 Å neutrons; open: 4.8 Å neutrons), K-7,8-C₂B₉H₁₂ (500 K, red symbols, filled: 9 Å neutrons; open: 4.8 Å neutrons), and K-7,9-C₂B₉H₁₂ (550 K, green filled symbols, 9 Å neutrons) compared with calculated model curves for different reorientational mechanisms: uniaxial 5-fold jumps (blue line: 7-CB₁₀H₁₃; green line: 7,8-C₂B₉H₁₂ and 7,9-C₂B₉H₁₂); uniaxial rotational diffusion (blue dashed line: K-7-CB₁₀H₁₃; green dashed line: 7,8-C₂B₉H₁₂ and 7,9-C₂B₉H₁₂); icosahedral tumbling (red dotted line: 7,8-C₂B₉H₁₂ and 7,9-C₂B₉H₁₂; light blue dotted line: 7-CB₁₀H₁₃); and isotropic rotational diffusion (red line: 7,8-C₂B₉H₁₂ and 7,9-C₂B₉H₁₂; light blue line: 7-CB₁₀H₁₃). Also included are calculated model curves for 7-CB₁₀H₁₃ assuming a different quasi-C₅-symmetric reorientational axis passing through the carbon apex (uniaxial 5-fold jumps: gray line; uniaxial rotational diffusion: gray dashed line). See the Supporting Information for model details.

compared with calculated models for uniaxial 5-fold jump reorientations, icosahedral tumbling, and both uniaxial and isotropic rotational diffusion of the anions. Unfortunately, reliable EISF data for disordered cubic β -KB₁₁H₁₄ could not be obtained from the 413 K QENS measurements, due to the presence of some substantial amount of ordered triclinic α -KB₁₁H₁₄ still persisting at this temperature. Somewhat higher temperatures are required to convert all the remaining α -KB₁₁H₁₄ to β -KB₁₁H₁₄, which were discouraged by the need for prolonged measurement times that would likely cause a gradual decomposition of the compound.

For the sake of simplicity, the uniaxial axis was chosen to be the quasi-C₅-symmetric axis perpendicular to the open-nest aperture of the *nido*-anions, although we have included two model curves for 7-CB₁₀H₁₃ (in gray) with a different reorientation axis passing through the carbon apex to demonstrate that reorientations around another preferred axis lead only to minor changes in the corresponding EISF and only above $Q \approx 1.5 \text{ \AA}^{-1}$.⁴⁷ Similarly, the EISFs for icosahedral tumbling and isotropic rotational diffusion are largely indistinguishable below $Q \approx 1.5 \text{ \AA}^{-1}$. The expressions representing the various model curves are included in the Supporting Information. Similarly, the EISF model differences between uniaxial 5-fold jump reorientations and uniaxial rotational diffusion and between icosahedral tumbling and isotropic rotational diffusion are largely absent below $Q \approx 1.5 \text{ \AA}^{-1}$, only becoming pronounced above this Q value. The

expressions representing the various model curves are included in the Supporting Information.

It is apparent from Figure 7 that the EISF data for the various *nido*-compounds are already dipping below the predicted uniaxial jump model curves at 500–550 K. This suggests that the anions in these compounds at these temperatures are already reorienting themselves to various degrees around different anion axes. Similar EISF behaviors were reported for the disordered phases of *nido*-Na-7-CB₁₀H₁₃⁴⁷ and *closo*-KCB₁₁H₁₂,³⁹ with the latter compound results more clearly indicating a progression toward more multiaxial reorientations with increasing temperatures.

A comparison of the EISFs for the three compounds in Figure 7 suggests differences in the multidimensionality of their respective anion reorientations, with K-7,9-C₂B₉H₁₂ displaying behavior closer to uniaxial than K-7,8-C₂B₉H₁₂ and K-7-CB₁₀H₁₃, even though its relative temperature is 50 K higher. Compared to more intermediate behavior for K-7-CB₁₀H₁₃, K-7,8-C₂B₉H₁₂ clearly exhibits anion reorientational motions already very close to isotropic rotational diffusion, with its behavior at the highest Q values much less in agreement with the EISF model curve for more-well-defined icosahedral tumbling motions. It should be noted that, despite these differences in reorientational behavior, all three anions exhibit similar fundamental jumping frequencies as displayed in Figure 6. Moreover, these rapid anion reorientational motions in the disordered phases, whether more uniaxial or highly multiaxial, are essential facilitators of increased cation translational mobility.¹³

Potassium Ionic Conductivity. The potassium ionic conductivities of KB₁₁H₁₄, K-7-CB₁₀H₁₃, K-7,8-C₂B₉H₁₂, and K-7,9-C₂B₉H₁₂ were determined from electrochemical impedance spectroscopy and are compared in Figure 8. The ionic

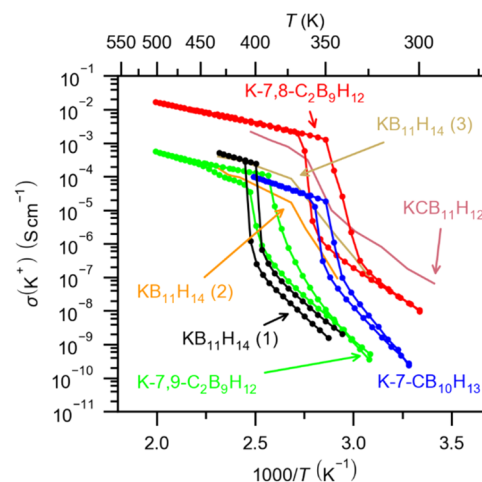


Figure 8. Potassium ionic conductivity data of the potassium *nido*-(carba)borates. The data on KB₁₁H₁₄ (1) are from this study, and the data on KB₁₁H₁₄ (2) and (3) are from ref 38 where KB₁₁H₁₄ (3) is a ball-milled sample. The data on KCB₁₁H₁₂ are from ref 39.

conductivities of all four compounds are hysteretic, with the highly conducting states retained upon cooling to temperatures lower than the initial transition temperatures upon heating, consistent with the FWS data as well as the behavior of numerous other metal *closo*- and *nido*-(carba)borates.^{15–18,39}

The ionic conductivities of as-synthesized and ball-milled KB₁₁H₁₄ have previously been reported by Souza et al. to be

$\sigma(K^+) = 1.2 \cdot 10^{-4}$ and $\sim 3.5 \cdot 10^{-4}$ S cm⁻¹, respectively, at 423 K.³⁸ Additionally, the two compounds have been reported to have high activation energies of $E_a = 1.9$ and 1.5 eV, respectively. Here, we observe a significantly different ionic conductivity behavior of commercial KB₁₁H₁₄. Below 395 K, the activation energy is 1.1 eV. A distinct polymorphic transition is observed in the temperature range ~ 400 –410 K, consistent with the FWS data. In the high-temperature, disordered phase, the activation energy decreases to 0.38 eV, and an ionic conductivity of $\sigma(K^+) = 4.3 \cdot 10^{-4}$ S cm⁻¹ is reached at 423 K, comparable to the ionic conductivity of the previously reported ball-milled KB₁₁H₁₄.³⁸ The disordered structure is retained to 400 K during cooling and subsequently reverts to the ordered polymorph with low ionic conductivity.

The ionic conductivity behaviors of the three remaining compounds are also consistent with the dynamical transitions observed in the FWS data. K-7-CB₁₀H₁₃ has a distinct phase transition in the temperature range ~ 345 –360 K. The activation energy decreases from 1.2 to 0.42 eV, and ionic conductivities of $\sigma(K^+) = 2.7 \cdot 10^{-5}$ and $1.0 \cdot 10^{-4}$ S cm⁻¹ are observed at 362 and 400 K, respectively. The disordered structure is retained to 350 K during cooling before reverting to the ordered phase. Similarly, K-7,8-C₂B₉H₁₂ has a phase transition in the temperature range ~ 350 –370 K and a decrease in activation energy from 0.81 to 0.28 eV. At 372 K, just above the phase transition, the ionic conductivity is $2.3 \cdot 10^{-2}$ S cm⁻¹ and at 500 K the ionic conductivity is $1.7 \cdot 10^{-2}$ S cm⁻¹, which makes K-7,8-C₂B₉H₁₂ the potassium electrolyte with the highest ionic conductivity above 350 K.

The potassium ionic conductivity behavior of K-7,9-C₂B₉H₁₂ is slightly different from the rest of the potassium *nido*-(carba)borates, consistent with both the FWS and *in situ* SRPKD data. A distinct phase transition is observed in the ionic conductivity data in the temperature range ~ 390 –410 K. However, two temperature ranges with different activation energies are observed above 410 K. In the low-temperature, ordered polymorph, α -K-7,9-C₂B₉H₁₂, the activation energy is 1.1 eV. Following the transition to the hexagonal structure, β -K-7,9-C₂B₉H₁₂, the activation energy decreases to 0.55 eV. However, with the second-order phase transition to the fully disordered phase, γ -K-7,9-C₂B₉H₁₂, above 450 K, the activation energy decreases even further to 0.28 eV, similar to the disordered phase of K-7,8-C₂B₉H₁₂. At 410 K, just above the first phase transition, the ionic conductivity is $\sigma(K^+) = 5.8 \cdot 10^{-5}$ S cm⁻¹, at 452 K, just above the second phase transition, the ionic conductivity is $2.3 \cdot 10^{-4}$ S cm⁻¹, and at 500 K the ionic conductivity is $5.6 \cdot 10^{-4}$ S cm⁻¹.

Notably, K-7,8-C₂B₉H₁₂ has an ionic conductivity more than 30 times higher than K-7,9-C₂B₉H₁₂. The two compounds both have an activation energy of 0.28 eV in their disordered states, which is 0.1 and 0.18 eV lower than the activation energies of Na-7,8-C₂B₉H₁₂ and Na-7,9-C₂B₉H₁₂, respectively. The low activation energies and especially the high ionic conductivity of K-7,8-C₂B₉H₁₂ supports that the higher carbon substitution in the anion cages favors mobility of the larger K⁺ compared to Na⁺, as Na-7,8-C₂B₉H₁₂ and Na-7,9-C₂B₉H₁₂ have the lowest ionic conductivities of the sodium *nido*-(carba)borates.¹⁴ Na impurities in K-7,8-C₂B₉H₁₂ can be ruled out based on the inductively coupled plasma optical emission spectrometry results presented in Table S1. It does seem counterintuitive that disordered cubic K-7,8-C₂B₉H₁₂, which has the smallest unit cell volume relative to the other three disordered cubic compounds, should exhibit the highest K⁺

ionic conductivity. This suggests that there are other factors responsible for this behavior. One possibility, which is hinted at by the QENS results, is that K⁺ migration may be enhanced in three dimensions by the more isotropic multidimensional reorientational motions of the 7,8-C₂B₉H₁₂⁻ anions compared to the other anions. One might expect that the isotropic reorientations of 7,8-C₂B₉H₁₂⁻ anions in all possible directions would also better enable the migration of K⁺ cations to different octahedral sites. In contrast, for compounds with more uniaxial anion reorientations, the K⁺ cation motions might be more directionally restricted. It should be further noted that the nest-hydrogen on 7,8-C₂B₉H₁₂⁻ is likely fluxional; i.e., it can rapidly move between two energetically favorable positions with a low activation barrier, which is not possible for the nest-hydrogens on 7-CB₁₀H₁₃⁻ and 7,9-C₂B₉H₁₂⁻. This fluxionality of the nest-hydrogen on 7,8-C₂B₉H₁₂⁻ may be one of the reasons for the more isotropic reorientational motions of the anion, and may also flatten the energy landscape for the cation migration because of the slightly greater flexibility of the structure and the directionality of the anion charge. One caveat is that, although the three nest-hydrogens of B₁₁H₁₄⁻ are also known to be fluxional,⁴⁸ we do not observe a similar enhancement in ionic conductivity for KB₁₁H₁₄ as for K-7,8-C₂B₉H₁₂. Based on the present experimental results, future molecular dynamics simulations as previously performed for LiCB₁₁H₁₂ and NaCB₁₁H₁₂¹³ may elucidate these phenomena better.

CONCLUSIONS

This work shows that the four potassium *nido*-(carba)borates KB₁₁H₁₄, K-7-CB₁₀H₁₃, K-7,8-C₂B₉H₁₂, and K-7,9-C₂B₉H₁₂ all undergo first-order polymorphic transitions from low-temperature, ordered structures to high-temperature, disordered structures with high ionic conductivities, similar to other metal *closo*- and *nido*-(carba)borates. For all four compounds, the disordered high-temperature polymorphs have cubic structures, where the anions are orientationally disordered. Additionally, K-7,9-C₂B₉H₁₂ has an intermediate phase with a trigonal unit cell in the temperature range ~ 450 to ~ 500 K. There is good agreement among the DSC data, the observed crystallographic phase transitions, the quasielastic neutron scattering fixed window scans, and the ionic conductivity data. The fixed window scans show that the hydrogen jumps in all four compounds increase from $\sim 10^8$ jumps s⁻¹ to at least the probing limit of $\sim 10^{10}$ jumps s⁻¹. Consequently, the high ionic conductivities are concomitant with fast reorientational dynamics of the anion cages. The reorientational activation energies of the anions in K-7-CB₁₀H₁₃, K-7,8-C₂B₉H₁₂, and K-7,9-C₂B₉H₁₂ were determined to be 0.151(2), 0.146(32), and 0.143(3) eV, respectively. The ionic conductivity activation energies in the high-temperature phases are 0.38, 0.42, 0.28, and 0.28 eV for KB₁₁H₁₄, K-7-CB₁₀H₁₃, K-7,8-C₂B₉H₁₂, and K-7,9-C₂B₉H₁₂, respectively. Notably, these activation energies are similar to or lower than the equivalent sodium *nido*-(carba)borates.¹⁴ While there is a clear trend in the ionic conductivities of the sodium *nido*-(carba)borates, i.e., lower ionic conductivity with increasing carbon substitution in the anion cage, there is no clear trend for the potassium *nido*-(carba)borates. The highest ionic conductivity is observed for K-7,8-C₂B₉H₁₂, which has an ionic conductivity of $1.7 \cdot 10^{-2}$ S cm⁻¹ at 500 K, which is more than 30 times higher than the ionic conductivity of K-7,9-C₂B₉H₁₂ at the same temperature. Both K-7-CB₁₀H₁₃ and K-7,8-C₂B₉H₁₂ transition to their high-

temperature polymorphs at significantly lower temperatures than $\text{KB}_{11}\text{H}_{14}$ and $\text{K-7,9-C}_2\text{B}_9\text{H}_{12}$. This shows that the ionic conductivity is highly dependent on the cation, the local anion charge and structure, the local interactions between the cation and the various anion cages, and the influence of anion reorientational behavior. Furthermore, relatively small changes in the anion has a large impact on the cation conductivity as seen when comparing the conductivities of $\text{K-7,8-C}_2\text{B}_9\text{H}_{12}$ and $\text{K-7,9-C}_2\text{B}_9\text{H}_{12}$. The present experimental study lays the groundwork for future molecular dynamics studies, which may elucidate the influence of the size and charge density of the cation as well as the local anion charge and structure on the local interactions in the crystal structures. This may also provide a better understanding of the ionic conduction mechanisms, which can facilitate better rational design of future metal hydridoborate-based solid-state electrolytes.

The promising results of especially $\text{K-7,8-C}_2\text{B}_9\text{H}_{12}$ suggests the possibility of stabilizing the high ionic conductivity to lower temperatures via strategies such as anion-mixing,^{5,7} ball-milling,^{21,49} nanoscaffold infiltration,²⁰ or complexation with molecular ligands.⁵⁰ With $\text{K-7,8-C}_2\text{B}_9\text{H}_{12}$ being one of the better solid-state potassium-ion conductors, there are prospects of the compound being a relevant electrolyte for solid-state potassium batteries. As suggested previously for *closo*- $\text{KCB}_{11}\text{H}_{12}$,³⁹ one might improve the K^+ conductivity further in this compound by substituting a small fraction of K^+ with larger cations such as Rb^+ or Cs^+ , to expand the disordered lattice and, in turn, decrease the interstitial steric restrictions to K^+ translational diffusion. Alternatively, the disordered lattice may possibly be expanded by substituting some *nido*-anions with even larger poly(carba)borate anions. In any case, further electrochemical studies are necessary to elucidate the electrochemical stability of the electrolytes as well as the compatibility with various cathodes and anodes. Through the realization of an electrochemically stable electrolyte with a high ionic conductivity at low temperatures, the development of a practical solid-state potassium battery operational at room temperature may be possible.

■ ASSOCIATED CONTENT

SI Supporting Information

The Supporting Information is available free of charge at <https://pubs.acs.org/doi/10.1021/acs.chemmater.5c00151>.

Nuclear magnetic resonance spectroscopy data, inductively coupled plasma optical emission spectrometry data, Structural determination and Rietveld refinements, *in situ* synchrotron radiation powder X-ray diffraction data, quasielastic neutron scattering results, ionic conductivity activation energy results (PDF)

Crystallographic information (CIFs) for $\text{KB}_{11}\text{H}_{14}$, $\text{K-7-CB}_{10}\text{H}_{13}$, $\text{K-7,8-C}_2\text{B}_9\text{H}_{12}$, and $\text{K-7,9-C}_2\text{B}_9\text{H}_{12}$ (ZIP)

Phonon animation files of $\text{KB}_{11}\text{H}_{14}$, $\text{K-7-CB}_{10}\text{H}_{13}$, $\text{K-7,8-C}_2\text{B}_9\text{H}_{12}$, and $\text{K-7,9-C}_2\text{B}_9\text{H}_{12}$ (ZIP)

■ AUTHOR INFORMATION

Corresponding Authors

Mads B. Amdisen – *Interdisciplinary Nanoscience Center (iNANO) and Department of Chemistry, Aarhus University, 8000 Aarhus C, Denmark; NIST Center for Neutron Research, National Institute of Standards and Technology, Gaithersburg, Maryland 20899-6102, United States;*

orcid.org/0000-0003-2663-8988; Email: mba@inano.au.dk

Hui Wu – *NIST Center for Neutron Research, National Institute of Standards and Technology, Gaithersburg, Maryland 20899-6102, United States; Email: hui.wu@nist.gov*

Authors

Mikael S. Andersson – *Department of Chemistry—Ångström Laboratory, Uppsala University, SE-751 21 Uppsala, Sweden; orcid.org/0000-0002-7119-0951*

Mirjana Dimitrievska – *NIST Center for Neutron Research, National Institute of Standards and Technology, Gaithersburg, Maryland 20899-6102, United States; National Renewable Energy Laboratory, Golden, Colorado 80401, United States; Transport at Nanoscale Interfaces Laboratory, Swiss Federal Laboratories for Material Science and Technology (EMPA), 8600 Duebendorf, Switzerland; orcid.org/0000-0002-9439-1019*

Wei Zhou – *NIST Center for Neutron Research, National Institute of Standards and Technology, Gaithersburg, Maryland 20899-6102, United States*

Torben R. Jensen – *Interdisciplinary Nanoscience Center (iNANO) and Department of Chemistry, Aarhus University, 8000 Aarhus C, Denmark; orcid.org/0000-0002-4278-3221*

Craig M. Brown – *NIST Center for Neutron Research, National Institute of Standards and Technology, Gaithersburg, Maryland 20899-6102, United States; orcid.org/0000-0002-9637-9355*

Juscelino B. Leão – *NIST Center for Neutron Research, National Institute of Standards and Technology, Gaithersburg, Maryland 20899-6102, United States; orcid.org/0000-0003-4015-535X*

Terrence J. Udovic – *NIST Center for Neutron Research, National Institute of Standards and Technology, Gaithersburg, Maryland 20899-6102, United States; Department of Materials Science and Engineering, University of Maryland, College Park, Maryland 20742, United States; orcid.org/0000-0002-9453-2483*

Complete contact information is available at:

<https://pubs.acs.org/doi/10.1021/acs.chemmater.5c00151>

Author Contributions

The manuscript was written through contributions of all authors. All authors have given approval to the final version of the manuscript.

Notes

The authors declare no competing financial interest.

■ ACKNOWLEDGMENTS

The work was supported by the Danish Council for Independent Research, Nature and Universe (Danskatt), and Technology and Production (CaMBat, DFF 0217-00327B). Affiliation with the Center for Integrated Materials Research (iMAT) at Aarhus University is gratefully acknowledged. Funding from the Danish Ministry of Higher Education and Science through the SMART Lighthouse is gratefully acknowledged. The authors gratefully acknowledge Dr. B. A. Trump for assistance with the SRPXD measurements. M.S.A. acknowledges the support from the ÅForsk Foundation (21-453) and the Göran Gustafsson Foundation. We acknowledge the MAX

IV Laboratory for beamtime on the DanMAX beamline under proposal 20230301. Research conducted at MAX IV, a Swedish national user facility, is supported by Vetenskapsrådet (Swedish Research Council, VR) under contract 2018-07152, Vinnova (Swedish Governmental Agency for Innovation Systems) under contract 2018-04969 and Formas under contract 2019-02496. DanMAX is funded by the NUFFI grant no. 4059-00009B. Access to the HFBS was provided by the Center for High Resolution Neutron Scattering, a partnership between the National Institute of Standards and Technology and the National Science Foundation under Agreement DMR-2010792. Powder X-ray diffraction experiments were performed on Beamline 17-BM-B at the Advanced Photon source, a U.S. Department of Energy Office of Science User Facility operated by Argonne National Laboratory, supported by the U.S. Department of Energy Office of Basic Energy Sciences (DE-AC02-06CH11357).

ADDITIONAL NOTE

¹Certain commercial equipment, instruments, or materials are identified in this document. Such identification does not imply recommendation or endorsement by the National Institute of Standards and Technology, nor does it imply that the products identified are necessarily the best available for the purpose.

REFERENCES

- (1) Schmaltz, T.; Hartmann, F.; Wicke, T.; Weymann, L.; Neef, C.; Janek, J. A Roadmap for Solid-State Batteries. *Adv. Energy Mater.* **2023**, *13* (43), No. 2301886.
- (2) Janek, J.; Zeier, W. G. Challenges in Speeding up Solid-State Battery Development. *Nat. Energy* **2023**, *8* (3), 230–240.
- (3) Matsuo, M.; Nakamori, Y.; Orimo, S. I.; Maekawa, H.; Takamura, H. Lithium Superionic Conduction in Lithium Borohydride Accompanied by Structural Transition. *Appl. Phys. Lett.* **2007**, *91* (22), No. 224103.
- (4) Cuevas, F.; Amdisen, M. B.; Baricco, M.; Buckley, C. E.; Cho, Y. W.; De Jongh, P.; De Kort, L. M.; Grinderslev, J. B.; Gulino, V.; Hauback, B. C.; Heere, M.; Humphries, T.; Jensen, T. R.; Kim, S.; Kisu, K.; Lee, Y.-S.; Li, H.-W.; Mohtadi, R.; Møller, K. T.; Ngene, P.; Noréus, D.; Orimo, S.; Paskevicius, M.; Polanski, M.; Sartori, S.; Skov, L. N.; Sørby, M. H.; Wood, B. C.; Yartys, V. A.; Zhu, M.; Latroche, M. Metallic and Complex Hydride-Based Electrochemical Storage of Energy. *Prog. Energy* **2022**, *4* (3), No. 032001.
- (5) Payandeh, S.; Asakura, R.; Avramidou, P.; Rentsch, D.; Łodziana, Z.; Černý, R.; Remhof, A.; Battaglia, C. Nido-Borate/Closo-Borate Mixed-Anion Electrolytes for All-Solid-State Batteries. *Chem. Mater.* **2020**, *32* (3), 1101–1110.
- (6) Asakura, R.; Duchêne, L.; Kühnel, R.-S.; Remhof, A.; Hagemann, H.; Battaglia, C. Electrochemical Oxidative Stability of Hydroborate-Based Solid-State Electrolytes. *ACS Appl. Energy Mater.* **2019**, *2* (9), 6924–6930.
- (7) Tang, W. S.; Yoshida, K.; Soloninin, A. V.; Skoryunov, R. V.; Babanova, O. A.; Skripov, A. V.; Dimitrievska, M.; Stavila, V.; Orimo, S.; Udovic, T. J. Stabilizing Superionic-Conducting Structures via Mixed-Anion Solid Solutions of Monocarba-Closo-Borate Salts. *ACS Energy Lett.* **2016**, *1* (4), 659–664.
- (8) Kim, S.; Oguchi, H.; Toyama, N.; Sato, T.; Takagi, S.; Otomo, T.; Arunkumar, D.; Kuwata, N.; Kawamura, J.; Orimo, S. A Complex Hydride Lithium Superionic Conductor for High-Energy-Density All-Solid-State Lithium Metal Batteries. *Nat. Commun.* **2019**, *10* (1), No. 1081.
- (9) Braun, H.; Asakura, R.; Remhof, A.; Battaglia, C. Hydroborate Solid-State Lithium Battery with High-Voltage NMC811 Cathode. *ACS Energy Lett.* **2024**, *9* (2), 707–714.
- (10) Asakura, R.; Reber, D.; Duchêne, L.; Payandeh, S.; Remhof, A.; Hagemann, H.; Battaglia, C. 4 V Room-Temperature All-Solid-State Sodium Battery Enabled by a Passivating Cathode/Hydroborate Solid Electrolyte Interface. *Energy Environ. Sci.* **2020**, *13* (12), 5048–5058.
- (11) Lu, Z.; Ciucci, F. Metal Borohydrides as Electrolytes for Solid-State Li, Na, Mg, and Ca Batteries: A First-Principles Study. *Chem. Mater.* **2017**, *29* (21), 9308–9319.
- (12) Deysheer, G.; Oh, J. A. S.; Chen, Y.-T.; Sayahpour, B.; Ham, S.-Y.; Cheng, D.; Ridley, P.; Cronk, A.; Lin, S. W.-H.; Qian, K.; Nguyen, L. H. B.; Jang, J.; Meng, Y. S. Design Principles for Enabling an Anode-Free Sodium All-Solid-State Battery. *Nat. Energy* **2024**, *9*, 1161–1172.
- (13) Dimitrievska, M.; Shea, P.; Kweon, K. E.; Bercx, M.; Varley, J. B.; Tang, W. S.; Skripov, A. V.; Stavila, V.; Udovic, T. J.; Wood, B. C. Carbon Incorporation and Anion Dynamics as Synergistic Drivers for Ultrafast Diffusion in Superionic LiCB₁₁H₁₂ and NaCB₁₁H₁₂. *Adv. Energy Mater.* **2018**, *8* (15), No. 1703422.
- (14) Tang, W. S.; Dimitrievska, M.; Stavila, V.; Zhou, W.; Wu, H.; Talin, A. A.; Udovic, T. J. Order–Disorder Transitions and Superionic Conductivity in the Sodium Nido-Undeca(Carba)Borates. *Chem. Mater.* **2017**, *29* (24), 10496–10509.
- (15) Tang, W. S.; Matsuo, M.; Wu, H.; Stavila, V.; Zhou, W.; Talin, A. A.; Soloninin, A. V.; Skoryunov, R. V.; Babanova, O. A.; Skripov, A. V.; Unemoto, A.; Orimo, S.; Udovic, T. J. Liquid-Like Ionic Conduction in Solid Lithium and Sodium Monocarba-Closo-Decaborates Near or at Room Temperature. *Adv. Energy Mater.* **2016**, *6* (8), No. 1502237.
- (16) Tang, W. S.; Unemoto, A.; Zhou, W.; Stavila, V.; Matsuo, M.; Wu, H.; Orimo, S.; Udovic, T. J. Unparalleled Lithium and Sodium Superionic Conduction in Solid Electrolytes with Large Monovalent Cage-like Anions. *Energy Environ. Sci.* **2015**, *8* (12), 3637–3645.
- (17) Udovic, T. J.; Matsuo, M.; Tang, W. S.; Wu, H.; Stavila, V.; Soloninin, A. V.; Skoryunov, R. V.; Babanova, O. A.; Skripov, A. V.; Rush, J. J.; Unemoto, A.; Takamura, H.; Orimo, S. Exceptional Superionic Conductivity in Disordered Sodium Decahydro-Closo-Decaborate. *Adv. Mater.* **2014**, *26* (45), 7622–7626.
- (18) Udovic, T. J.; Matsuo, M.; Unemoto, A.; Verdal, N.; Stavila, V.; Skripov, A. V.; Rush, J. J.; Takamura, H.; Orimo, S. Sodium Superionic Conduction in Na₂B₁₂H₁₂. *Chem. Commun.* **2014**, *50* (28), 3750–3752.
- (19) Møller, K. T.; Paskevicius, M.; Andreassen, J. G.; Lee, J.; Chen-Tan, N.; Overgaard, J.; Payandeh, S.; Silvester, D. S.; Buckley, C. E.; Jensen, T. R. Molten Metal Closo-Borate Solvates. *Chem. Commun.* **2019**, *55* (23), 3410–3413.
- (20) Andersson, M. S.; Stavila, V.; Skripov, A. V.; Dimitrievska, M.; Psurek, M. T.; Leão, J. B.; Babanova, O. A.; Skoryunov, R. V.; Soloninin, A. V.; Karlsson, M.; Udovic, T. J. Promoting Persistent Superionic Conductivity in Sodium Monocarba-Closo-Dodecaborate NaCB₁₁H₁₂ via Confinement within Nanoporous Silica. *J. Phys. Chem. C* **2021**, *125* (30), 16689–16699.
- (21) Murgia, F.; Brighi, M.; Piveteau, L.; Avalos, C. E.; Gulino, V.; Nierstenhöfer, M. C.; Ngene, P.; De Jongh, P.; Černý, R. Enhanced Room-Temperature Ionic Conductivity of NaCB₁₁H₁₂ via High-Energy Mechanical Milling. *ACS Appl. Mater. Interfaces* **2021**, *13* (51), 61346–61356.
- (22) Gulino, V.; Longo, A.; De Kort, L. M.; Rodenburg, H. P.; Murgia, F.; Brighi, M.; Černý, R.; Sahle, C. J.; Sundermann, M.; Gretarsson, H.; De Groot, F.; Ngene, P. Anomalous Impact of Mechanochemical Treatment on the Na-ion Conductivity of Sodium Closo-Carbadodecaborate Probed by X-Ray Raman Scattering Spectroscopy. *Small Methods* **2024**, *8* (1), No. 2300833.
- (23) The mention of all commercial suppliers in this paper is for clarity and does not imply the recommendation or endorsement of these suppliers by NIST.
- (24) Toby, B. H.; Von Dreele, R. B. GSAS-II: The Genesis of a Modern Open-Source All Purpose Crystallography Software Package. *J. Appl. Crystallogr.* **2013**, *46* (2), 544–549.
- (25) Rietveld, H. M. A Profile Refinement Method for Nuclear and Magnetic Structures. *J. Appl. Crystallogr.* **1969**, *2* (2), 65–71.

- (26) Larson, A. C.; Von Dreele, R. B.; Report LAUR 86–748. *General Structure Analysis System* Los Alamos National Laboratory: NM; 1994.
- (27) Udovic, T. J.; Brown, C. M.; Leão, J. B.; Brand, P. C.; Jiggetts, R. D.; Zeitoun, R.; Pierce, T. A.; Peral, I.; Copley, J. R. D.; Huang, Q.; Neumann, D. A.; Fields, R. J. The Design of a Bismuth-Based Auxiliary Filter for the Removal of Spurious Background Scattering Associated with Filter-Analyzer Neutron Spectrometers. *Nucl. Instrum. Methods A* **2008**, *588* (3), 406–413.
- (28) Meyer, A.; Dimeo, R. M.; Gehring, P. M.; Neumann, D. A. The High-Flux Backscattering Spectrometer at the NIST Center for Neutron Research. *Rev. Sci. Instrum.* **2003**, *74* (5), 2759–2777.
- (29) Copley, J. R. D.; Cook, J. C. The Disk Chopper Spectrometer at NIST: A New Instrument for Quasielastic Neutron Scattering Studies. *Chem. Phys.* **2003**, *292* (2–3), 477–485.
- (30) Azuah, R. T.; Kneller, L. R.; Qiu, Y.; Tregenna-Piggott, P. L. W.; Brown, C. M.; Copley, J. R. D.; Dimeo, R. M. DAVE: A Comprehensive Software Suite for the Reduction, Visualization, and Analysis of Low Energy Neutron Spectroscopic Data. *J. Res. Natl. Inst. Stand. Technol.* **2009**, *114* (6), No. 341.
- (31) Giannozzi, P.; Baroni, S.; Bonini, N.; Calandra, M.; Car, R.; Cavazzoni, C.; Ceresoli, D.; Chiarotti, G. L.; Cococcioni, M.; Dabo, I.; Dal Corso, A.; De Gironcoli, S.; Fabris, S.; Fratesi, G.; Gebauer, R.; Gerstmann, U.; Gougoussis, C.; Kokalj, A.; Lazzeri, M.; Martin-Samos, L.; Marzari, N.; Mauri, F.; Mazzarello, R.; Paolini, S.; Pasquarello, A.; Paulatto, L.; Sbraccia, C.; Scandolo, S.; Sclauzero, G.; Seitsonen, A. P.; Smogunov, A.; Umari, P.; Wentzcovitch, R. M. QUANTUM ESPRESSO: A Modular and Open-Source Software Project for Quantum Simulations of Materials. *J. Phys.:Condens. Matter* **2009**, *21* (39), No. 395502.
- (32) Kresse, G.; Furthmüller, J.; Hafner, J. *Ab Initio* Force Constant Approach to Phonon Dispersion Relations of Diamond and Graphite. *Europhys. Lett.* **1995**, *32* (9), 729–734.
- (33) Yildirim, T. Structure and Dynamics from Combined Neutron Scattering and First-Principles Studies. *Chem. Phys.* **2000**, *261*, 205–216.
- (34) Hosmane, N. S.; Wermer, J. R.; Hong, Z.; Getman, T. D.; Shore, S. G. High Yield Preparation of the Tetradehydrodecaborate(1-) Anion, $[B_{11}H_{14}]^-$, from Pentaborane(9). *Inorg. Chem.* **1987**, *26* (21), 3638–3639.
- (35) Wright, F.; Garber, R.; Todd, L. J. A ^{11}B NMR Study of Heteroatom Boranes of the Type $B_{10}H_{12}E$ ($E = CNMe_3, CH_3^-, PR, AsR, As^-, S, Se, and Te$). *J. Magn. Reson.* **1978**, *30* (3), 595–602.
- (36) Batsanov, A. S.; Fox, M. A.; Goeta, A. E.; Howard, J. A. K.; Hughes, A. K.; Malget, J. M. A Convenient Cyanide-Free “One-Pot” Synthesis of Nido- $Me_3N-7-CB_{10}H_{12}$ and Nido- $7-CB_{10}H_{13}^-$. *J. Chem. Soc., Dalton Trans.* **2002**, 2624–2631.
- (37) Fox, M. A.; Goeta, A. E.; Hughes, A. K.; Johnson, A. L. Crystal and Molecular Structures of the Nido-Carborane Anions, 7,9- and 2,9- $C_2B_9H_{12}^-$. *J. Chem. Soc., Dalton Trans.* **2002**, 2132–2141.
- (38) Souza, D. H. P.; Möller, K. T.; Moggach, S. A.; Humphries, T. D.; D’Angelo, A.; Buckley, C.; Paskevicius, M. Hydrated Alkali- $B_{11}H_{14}$ Salts as Potential Solid-State Electrolytes. *J. Mater. Chem. A* **2021**, *9*, 15027–15037.
- (39) Dimitrievska, M.; Wu, H.; Stavila, V.; Babanova, O. A.; Skoryunov, R. V.; Soloninin, A. V.; Zhou, W.; Trump, B. A.; Andersson, M. S.; Skripov, A. V.; Udovic, T. J. Structural and Dynamical Properties of Potassium Dodecahydro-Monocarbocloso-Dodecaborate: $KCB_{11}H_{12}$. *J. Phys. Chem. C* **2020**, *124* (33), 17992–18002.
- (40) Tiritiris, I.; Schleid, T. Die Dodecahydro-Closo-Dodecaborate $M_2[B_{12}H_{12}]$ Der Schwere Alkalimetalle ($M^+ = K^+, Rb^+, NH_4^+, Cs^+$) Und Ihre Formalen Iodid-Addukte $M_3I[B_{12}H_{12}]$ ($\equiv MI \cdot M_2[B_{12}H_{12}]$). *Z. Anorg. Allg. Chem.* **2003**, *629* (78), 1390–1402.
- (41) Wu, H.; Tang, W. S.; Zhou, W.; Tarver, J. D.; Stavila, V.; Brown, C. M.; Udovic, T. J. The Low-Temperature Structural Behavior of Sodium 1-Carba-Closo-Decaborate: $NaCB_9H_{10}$. *J. Solid State Chem.* **2016**, *243*, 162–167.
- (42) Verdál, N.; Zhou, W.; Stavila, V.; Her, J.-H.; Yousufuddin, M.; Yildirim, T.; Udovic, T. J. Alkali and Alkaline-Earth Metal Dodecahydro-Closo-Dodecaborates: Probing Structural Variations via Neutron Vibrational Spectroscopy. *J. Alloys Compd.* **2011**, *509*, S694–S697.
- (43) Phonon animation ascii files in the Supporting Information for the DFT-optimized 0 K ordered nido-compound structures can be viewed using the open-source v_sim software, https://gitlab.com/l_sim/v_sim-website/-/tree/master/download (accessed on 26th May 2023).
- (44) Frick, B.; Combet, J.; Van Eijck, L. New Possibilities with Inelastic Fixed Window Scans and Linear Motor Doppler Drives on High Resolution Neutron Backscattering Spectrometers. *Nucl. Instrum. Methods A* **2012**, *669*, 7–13.
- (45) Andersson, M. S.; Grinderslev, J. B.; Jensen, T. R.; García Sakai, V.; Häussermann, U.; Udovic, T. J.; Karlsson, M. Interplay of NH_4^+ and BH_4^- Reorientational Dynamics in NH_4BH_4 . *Phys. Rev. Mater.* **2020**, *4* (8), No. 085002.
- (46) Babanova, O. A.; Skoryunov, R. V.; Soloninin, A. V.; Skripov, A. V. Anion Reorientations and the Phase Transition in Nido- $KB_{11}H_{14}$: 1H and ^{11}B NMR Studies. *Iomics* **2022**, *28* (12), 5505–5512.
- (47) Skripov, A. V.; Majer, G.; Babanova, O. A.; Skoryunov, R. V.; Soloninin, A. V.; Dimitrievska, M.; Udovic, T. J. Na^+ Diffusivity in Carbon-Substituted Nido- and Closo-Hydroborate Salts: Pulsed-Field-Gradient NMR Studies of Na-7- $CB_{10}H_{13}$ and $Na_2(CB_9H_{10})-(CB_{11}H_{12})$. *J. Alloys Compd.* **2021**, *850*, No. 156781.
- (48) Maitre, P.; Eisenstein, O.; Michos, D.; Luo, X. L.; Siedle, A. R.; Wisniewski, L.; Zilm, K. W.; Crabtree, R. H. Borate Anion ($B_{11}H_{14}^-$): A Nido Cage with No Hydrogen...Hydrogen Interaction. *J. Am. Chem. Soc.* **1993**, *115* (17), 7747–7751.
- (49) Tang, W. S.; Matsuo, M.; Wu, H.; Stavila, V.; Unemoto, A.; Orimo, S.; Udovic, T. J. Stabilizing Lithium and Sodium Fast-Ion Conduction in Solid Polyhedral-Borate Salts at Device-Relevant Temperatures. *Energy Storage Mater.* **2016**, *4*, 79–83.
- (50) Lu, Z.; Qiu, P.; Zhai, H.; Zhang, G.; Chen, X.; Lu, Z.; Wu, Y.; Chen, X. Facile Synthesis of Potassium Decahydro-Monocarbocloso-Decaborate Imidazole Complex Electrolyte for All-Solid-State Potassium Metal Batteries. *Angew. Chem., Int. Ed.* **2024**, *63* (51), No. e202412401.